Lab-Scale Experimental Characterization and Dynamic Scaling Assessment for Closed-Loop Crosswind Flight of Airborne Wind Energy Systems

Mitchell Cobb
Department of Mechanical Engineering,
University of North Carolina at Charlotte,
Charlotte, NC 28223
e-mail: mcobb12@uncc.edu

Nihar Deodhar
Department of Mechanical Engineering,
University of North Carolina at Charlotte,
Charlotte, NC 28223
e-mail: ndeodhar@uncc.edu

Christopher Vermillion[1,2]
Department of Mechanical Engineering,
University of North Carolina at Charlotte,
Charlotte, NC 28223
e-mail: cvermill@uncc.edu

This paper presents the experimental validation and dynamic similarity analysis for a lab-scale version of an airborne wind energy (AWE) system executing closed-loop motion control. Execution of crosswind flight patterns, achieved in this work through the asymmetric motion of three tethers, enables dramatic increases in energy generation compared with stationary operation. Achievement of crosswind flight in the lab-scale experimental framework described herein allows for rapid, inexpensive, and dynamically scalable characterization of new control algorithms without recourse to expensive full-scale prototyping. We first present the experimental setup, then derive dynamic scaling relationships necessary for the lab-scale behavior to match the full-scale behavior. We then validate dynamic equivalence of crosswind flight over a range of different scale models of the Altaeros Buoyant airborne turbine (BAT). This work is the first example of successful lab-scale control and measurement of crosswind motion for an AWE system across a range of flow speeds and system scales. The results demonstrate that crosswind flight can achieve significantly more power production than stationary operation, while also validating dynamic scaling laws under closed-loop control. [DOI: 10.1115/1.4038650]

1 Introduction

Wind energy is one of several renewable energy sources that continue to play an increasing role in satisfying the world's energy demand. However, tower costs and installation logistics typically limit towered wind turbine installations to nonremote and shallow-water offshore locations. Furthermore, towers limit hub heights to approximately 100 m, which does not provide access to stronger high-altitude winds. Airborne wind energy (AWE) systems, which replace towers with tethers and a lifting body (a kite, wing, or aerostat), enable operation at altitudes up to 600 m, where winds are stronger and more consistent, all while eliminating up to 90% of the material required for towered systems (see Ref. [1]). Simultaneously, these systems produce power at a lower price to the consumer than diesel generators (see Refs. [2] and [3]). This makes AWE systems a good fit for remote and off-grid communities. Inspired by these possibilities, numerous companies and research organizations (see Refs. [1] and [4–9]) have pioneered unique designs for AWE systems over the past decade. Several AWE systems are depicted in Fig. 1. These systems either feature airborne power generation (as is the case with Refs. [1] and [5], where power is generated by an on-board turbine(s) and transmitted to the ground) or ground-based power generation (as is the case with Ref. [4], where power is generated on the ground as a result of tension in the tethers as they are spooled out).

In addition to enabling high-altitude operation, the replacement of a tower with tethers enables motion through the air. While this may initially be viewed as a drawback, appropriately designed periodic motions have been shown in Ref. [10] to significantly enhance the power output of an AWE system. Specifically, by flying an AWE system perpendicular to the wind direction, the apparent wind speed presented to the airborne system is increased. This motion, termed *crosswind* flight, translates into *significantly* increased power production, as the power production from a wind turbine is proportional to the apparent wind speed *cubed*. The promise of significantly increased energy generation has led to a growing body of literature that focuses on crosswind flight control algorithms, including [11–16].

The vast majority of existing literature on AWE system flight control has been simulation based. It is well established that while existing models capture the key variables and phenomena involved with AWE flight dynamics, they fall short of predicting significant dynamic characteristics [17,18]. The limitations of existing models arise from necessary model order reduction, use of lumped, steady aerodynamic models, and unknown model parameters.

Given the nascent state of AWE control systems, inaccuracies in existing simulation models, and significant full-scale experimental prototyping costs, an inexpensive, small-scale experimental framework for AWE system flight characterization is highly desirable. However, achieving such a framework in a way that is approximately dynamically scalable to full-scale systems is a challenging engineering feat. This has limited the number of efforts in the AWE community to develop a lab-scale framework.

Within the limited body of literature that addresses small-scale experimental characterization of crosswind systems, the authors of Ref. [19] built a *small*-scale (approximately 30 m maximum line length) system for characterizing and optimizing figure-eight crosswind motions. Meanwhile, the authors of Ref. [20] have developed a wind tunnel-based *lab*-scale experimental framework for a rotating cylinder that uses the Magnus effect to generate lift.

[1]Corresponding author.
[2]Present address: Altaeros Energies, Somerville, MA 02143.

Contributed by the Dynamic Systems Division of ASME for publication in the Journal of Dynamic Systems, Measurement, and Control. Manuscript received May 6, 2017; final manuscript received November 15, 2017; published online January 16, 2018. Assoc. Editor: Mazen Farhood.

(*a*) (*b*) (*c*)

Fig. 1 AWE systems that have been implemented at full scale, including the (*a*) KITEnrg system [4], (*b*) Altaeros BAT [5], and (*c*) Google-owned Makani Power prototype [1]

However, the use of a heavier-than-air model in a wind tunnel at this scale does not allow for dynamic similarity between lab-scale and full-scale flight, due to the tremendous resulting differences in characteristic oscillation frequencies.

The authors of Refs. [17], [18], and [21–24], on the other hand, have developed a *water channel*-based framework for lab-scale experimental characterization of AWE systems, with the goal of establishing dynamic similarity results between this lab-scale setup and its full-scale counterpart. Work in Refs. [17] and [18] proposed an initial framework necessary for measuring position and orientation of a lab-scale system during *passive* flight. This work was then extended in Refs. [21–23] to include active control to *constant* set points, resulting in nominally stationary flight. In order to implement crosswind flight at lab scale, a significantly enhanced motion capture system was introduced in Ref. [24] for the purpose of measuring model position and orientation over a much larger range of dynamic motions. This led to the first demonstration of lab-scale crosswind flight in Ref. [24], with an evaluation of crosswind flight over multiple flow conditions (and a single model) presented in Ref. [16].

While our previous conference publications [16,24] demonstrate successful crosswind flight under a limited number of flow conditions, these references focus on a single model, do not include a controller scaling analysis that demonstrates equivalence between lab-scale and full-scale, and do not account for the energy *consumed* in crosswind flight. In fact, all of the previous scaling analysis for the water channel system, which is summarized in Ref. [23], is restricted to the passive system, without consideration of control parameters. The present paper is the first to establish dynamic scaling results for control parameters, for both stationary and crosswind closed-loop flight. Thus, it serves as a greatly extended version of our previous conference results.

The contributions of this work are as follows:

- The first lab-scale demonstration of closed-loop crosswind flight at lab scale, for a variety of flow conditions and model scales.
- An enhanced motion capture system capable of operating under rapidly varying trajectories and lighting conditions.
- Dynamic scaling relationships that indicate how controller parameters need to be scaled to achieve similarity between lab-scale and full-scale flight.
- Experimental validation and error analysis of dynamic scaling laws under closed-loop crosswind flight control.
- Energy generation performance analysis.

After describing the full-scale system, dynamic model, and crosswind flight control strategy in Sec. 2, we detail the lab-scale system and present the augmented motion capture system in Sec. 3. Section 4 details the dynamic similarity between the lab-scale and full-scale systems, presenting scaling laws necessary to achieve dynamic similarity under closed-loop control. Results in Sec. 5 show that:

- Crosswind flight is effectively induced and controlled via this strategy;
- this crosswind flight can produce significant increases in energy generation performance; and
- dynamic behavior across three model scales obeys scaling laws derived via Buckingham-Pi analysis to within experimental tolerances.

We conclude with a discussion of possible sources of error inherent in the water channel setup.

2 Full-Scale System: Modeling and Flight Control

The various designs of AWE systems can be controlled though either active aerodynamic surfaces (as is the case with the Google-Based Makani Power [1] and Ampyx [6] systems, among others) or tether articulation (used by Altaeros Energies [5] and KITEnrg [4], among others). The control strategy utilized in this work induces crosswind motion through the asymmetric articulation of tethers. For this purpose, we focus specifically on the Altaeros Buoyant air turbine (BAT). The BAT, shown in Fig. 2, is a lighter-than-air design wherein a horizontal-axis turbine is suspended within an annular shell. The system is intended for flight at altitudes up to 600 m, where it can harness energy from strong and consistent winds. The BAT consists of four main components, namely, a helium-filled annular shroud that holds the turbine, the turbine itself, three tethers (one of which is a conductive cable), and a ground station. One tether is attached at the center of the

Fig. 2 Image of prototype full-scale system, the Altaeros BAT, showing annular shroud, turbine, tethers, and ground station (Adapted from Ref. [5])

rear (aft) of the lifting body. The other two are attached on either side (port and starboard) of the front of the lifting body. While the BAT is nominally designed for stationary flight, the cross section of the annular shell is composed of lifting airfoils, thereby producing the aerodynamic forces that make it possible to realize increased power generation under crosswind motion.

2.1 Dynamic Model. The dynamic scaling analysis described in this paper is based on a relatively simple model, discussed in Ref. [17], that captures the key variables involved in the AWE system but does not possess the fidelity of real flight experiments. Hence, the model contains the necessary information for conducting a dynamic scaling analysis; nevertheless, it is by no means a replacement for experiments.

The model of Ref. [17], which is derived using a Euler–Lagrange approach, approximates the three tethers as a single tether of length L_t and a spherical bridle joint as shown in Fig. 3. This approximation results in a model that is fully described by ordinary differential equations, without algebraic constraints. The model derived therein has the form

$$D(Q)\ddot{Q} + C(Q,\dot{Q})\dot{Q} + G(Q) = \tau(Q,\dot{Q},v_{\text{wind}},\psi_{\text{wind}}) \tag{1}$$

$$X = f(Q,\dot{Q}) \tag{2}$$

$$\Omega = g(Q,\dot{Q}) \tag{3}$$

where v_{wind} is the wind speed, ψ_{wind} is the wind heading, and

$$Q = [\Phi \quad \Lambda \quad \Psi \quad L_t \quad \theta' \quad \phi'] \tag{4}$$

$$X = [x_g \quad y_g \quad z_g \quad \dot{x}_b \quad \dot{y}_b \quad \dot{y}_b] \tag{5}$$

$$\Omega = [\phi \quad \theta \quad \psi \quad p \quad q \quad r] \tag{6}$$

The azimuth angle, Φ, zenith angle, Λ, tether twist angle, Ψ, and mean tether length, L_t, are shown in Fig. 3. The vector X includes the ground frame positions, denoted by the subscript "g," and the body frame translational velocities, denoted by the subscript "b." The vector Ω includes the rotational degrees-of-freedom (Euler angles), along with the body frame rotational velocities. The quantities θ' and ϕ' are termed the *induced* pitch and the induced roll, respectively. Along with yaw, they describe the orientation of the lifting body relative to its position vector. These angles are approximately related to the tether lengths by

$$\phi' = \tan^{-1}\left(\frac{l_3 - l_2}{l_{\text{sep}}^{\text{lat}}}\right) \tag{7}$$

$$\theta' = \tan^{-1}\left(\frac{l_1 - 0.5(l_2 + l_3)}{l_{\text{sep}}^{\text{long}}}\right) \tag{8}$$

where $l_{\text{sep}}^{\text{long}}$ and $l_{\text{sep}}^{\text{lat}}$ are longitudinal and lateral tether attachment separation distances, respectively. This approximation, wherein we model a three-tether system using a single link plus two rotational degrees-of-freedom, allows us to model the AWE system using ordinary differential equations, rather than differential algebraic equations. The control inputs are the tether release speeds, u_i, which are related to the tether lengths by

$$u_i = \frac{d}{dt} l_i \tag{9}$$

For the full-scale system, the tether speed commands are realized through a variable frequency drive system. For the lab-scale system, the tether release speed commands are realized through direct current (DC) motors whose input voltages are proportional to the tether release speeds.

2.2 Basic Flight Control. The goal of the BAT's control system is to use three tethers to impart desirable flight characteristics to the system. In the case of stationary flight, this involves using the three tethers to keep the altitude, pitch angle, and roll angle fixed at desirable values. For crosswind flight, detailed in Sec. 2.3, the side tethers will be used to periodically alter the roll angle setpoint for the purpose of power augmentation.

The use of three tethers enables direct control of three quantities. Pitch, θ, is controlled by spooling out on the aft tether while spooling in on the front tethers, or vice versa. Roll, ϕ, is controlled by spooling out on the port tether and spooling in on the starboard tether, or vice versa. Altitude, z_g, is controlled by spooling all tethers in or out simultaneously. Each of three controllers, namely, the altitude controller, pitch angle controller, and roll angle controller, is composed of a lead filter (i.e., a filtered proportional plus derivative controller). A block diagram of the control strategy is shown in Fig. 4. The individual controller transfer functions are

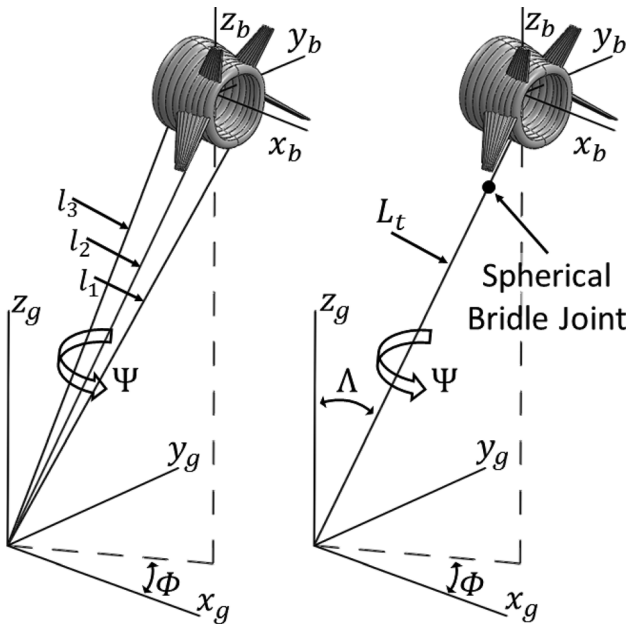

Fig. 3 Comparison of full-scale system (left) with dynamic model approximation (right) which treats the three-tether system as a single tether with a spherical bridle joint

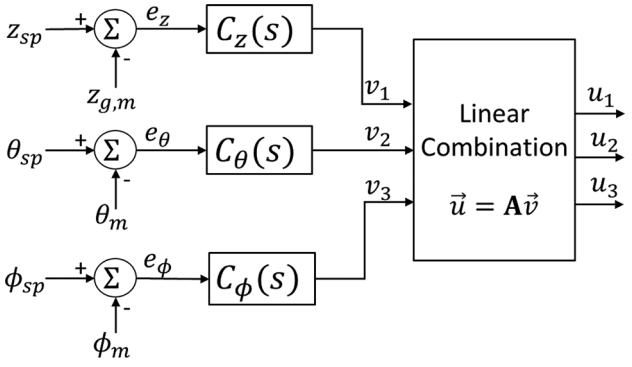

Fig. 4 Block diagram of the flight control strategy showing setpoints z_{sp}, θ_{sp}, and ϕ_{sp}, tether release speed commands, u_1, u_2, and u_3 as well as the measured altitude, pitch, and roll $z_{g,m}$, θ_m, and ϕ_m

$$C_z(s) = \frac{k_{dz}s + k_{pz}}{\tau_z s + 1}$$
$$C_\theta(s) = \frac{k_{d\theta}s + k_{p\theta}}{\tau_\theta s + 1} \tag{10}$$
$$C_\phi(s) = \frac{k_{d\phi}s + k_{p\phi}}{\tau_\phi s + 1}$$

The signals produced by the individual controllers are combined to produce tether release speed commands, which are related to v_1, v_2, and v_3 through a linear combination (see Fig. (4)) where

$$\mathbf{A} = \begin{bmatrix} 1 & -1 & 0 \\ 1 & 1 & 1 \\ 1 & 1 & -1 \end{bmatrix} \tag{11}$$

Because there exists a pure integrator between the motor voltage commands and the tether lengths (l_1, l_2, and l_3, which dictate r_z, θ, and ϕ), an integrator is not included in the controller itself, as it is unnecessary for tracking sufficiently slowly varying commands and would lead to reduced stability margins if included.

2.3 Crosswind Augmentation. The Altaeros BAT, which is used as a case study in this work, is designed for nominally stationary operation; thus, it does not possess the high lift/drag ratios and nimble dynamics of some other lifting bodies, which are required to realize several times as much power under crosswind flight than in stationary operation. Nevertheless, its annular design does allow for significant lift and side force, thereby allowing for moderately increased power production under crosswind motions.

During crosswind flight, the wind speed delivered to an airborne turbine, v_a, is a combination of the wind velocity vector $\mathbf{v}_f$ and the velocity vector of the turbine $\mathbf{v}$. It is computed by a simple vector difference. This is shown in Fig. 5 (left) and given by

$$v_a = |\mathbf{v}_f - \mathbf{v}| \tag{12}$$

To characterize the benefit of crosswind flight, it is beneficial to introduce a measure that compares the energy generation potential under crosswind motion to that which could be achieved under stationary operation with the same equipment. That comparison is quantitatively characterized in this work by the *power ratio*, P. The power ratio characterizes the amount of additional power that can be created by the crosswind motion as compared with the power that could be generated by the same turbine under stationary flight, assuming that the turbine is operating below its rated wind speed at all times. This ratio is given by

$$P(t) = \frac{P_{\text{Generated}}(t) - P_{\text{Control}}(t)}{P_{\text{Stationary}}(t)} = \frac{\frac{1}{2}\rho v_a^3 A_{\text{ref}} C_p - \sum_{i=1}^{3} k_w(u_i(t))\tau_i(t)u_i(t)}{\frac{1}{2}\rho v_f^3 A_{\text{ref}} C_p} \tag{13}$$

where ρ represents the fluid density, C_p represents the turbine's power coefficient, A_{ref} represents the rotor area, and τ_i represents individual tether tensions. The term $k_w(u_i(t))$ represents a lumped winch efficiency term (accounting for regenerative capabilities) given by

$$k_w(u_i(t)) = \begin{cases} -\dfrac{1}{\eta_m}, & u_i(t) < 0 \\ -\eta_g, & u_i(t) \geq 0 \end{cases} \tag{14}$$

where η_m and η_g represent the motor efficiency and regenerative efficiency, respectively.

To induce crosswind flight, the BAT is rolled to the side as shown in Fig. 5 (right). This results in a sideways component of the aerodynamic lift vector, causing the BAT to move laterally, thereby inducing crosswind motion. One method to implement this strategy is to hold z_{sp} and θ_{sp} constant, while ϕ_{sp} is varied periodically, according to a square wave profile given by

$$\phi_{sp}(t) = \begin{cases} a_0, & kT \leq t < kT + \dfrac{T}{2} \\ -a_0, & kT + \dfrac{T}{2} \leq t < (k+1)T \end{cases} \tag{15}$$

for $k \in \mathbb{N}$. The amplitude, a_0, and period, T, represent tunable parameters that have a significant impact on the energy that can be produced through crosswind flight trajectories.

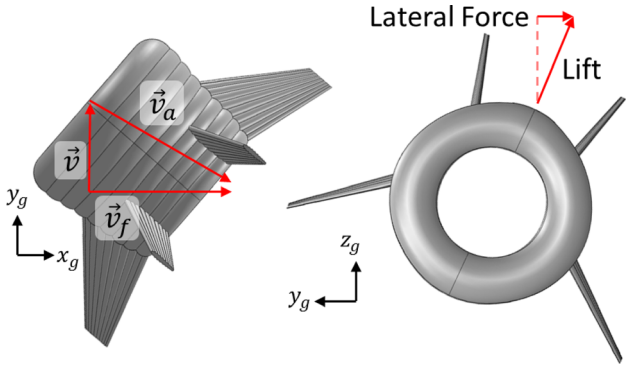

Fig. 5 Top-down (left) and frontal view of AWE system (right) depicting the method of inducing crosswind flight. The top-down view shows free stream velocity of fluid flow, $\mathbf{v}_f$, velocity vector of model, $\mathbf{v}$, and velocity vector of apparent wind as experienced by the model $\mathbf{v}_a$. The frontal view shows how the aerodynamic lift vector generates significant lateral force when the model is rolled.

3 Lab-Scale Experimental Setup

This work is based on a small-scale setup for characterizing the dynamics and control of an AWE system in a 1 m × 1 m *water channel*, as shown in Fig. 6. Three-dimensional (3D) printed models, whose cross-sectional areas comprise less than 1.5% of the total water channel cross-sectional area, are tethered and "flown" in the water channel. For the full-scale system, resolving position and orientation simply involves a global positioning system and inertial measurement unit. Since that equipment is impractical for a small-scale model in water, it was necessary to replace the motion capture system with a wholly different system. The method of motion capture presented here produces the same outputs as the full-scale system, namely, the position and orientation of the BAT. This makes it possible to accurately model the structure of the controller used at full scale. Figure 7 shows a detailed comparison between the control strategies of the full-scale and lab-scale systems.

During an experiment, an individual model is tethered and "flown" in the water channel experimental setup shown in Fig. 6. The experimental equipment consists of three DC motors for tether actuation, three high-speed cameras for image acquisition, and a high-performance host/target computer pair for real-time motion capture and closed-loop control. The motor time constants for the micro-DC motors used in this work are more than an order of magnitude faster than the desired closed-loop system time constants. The image processing and real-time controller are executed on a dedicated personal computer, using Mathworks (Natick, MA) SIMULINK Real-Time® software. The system uses Basler ACE 340 km grayscale cameras to obtain the images of the model.

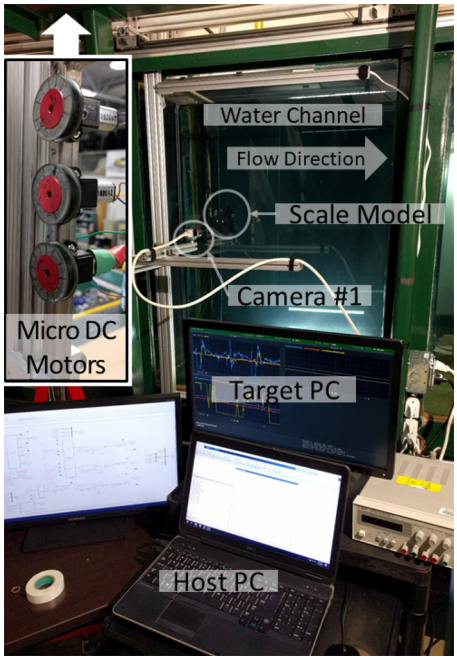

Fig. 6 Image of experimental equipment showing the water channel, host computer, target computer, DC motors (inset left), scale model, and video cameras. The DC motors and tether spools are located above the water channel, outside the frame of the main image.

The use of three cameras at different orientations (two perpendicular to the flow and one at a 45 deg "slant" underneath the water channel) provides sufficient imaging data for resolving both the position and orientation of the model. In this work, the model position vector, $\mathbf{r} = [x_g\ y_g\ z_g]$, points from the origin of the ground-fixed coordinate system to the origin of the body-fixed

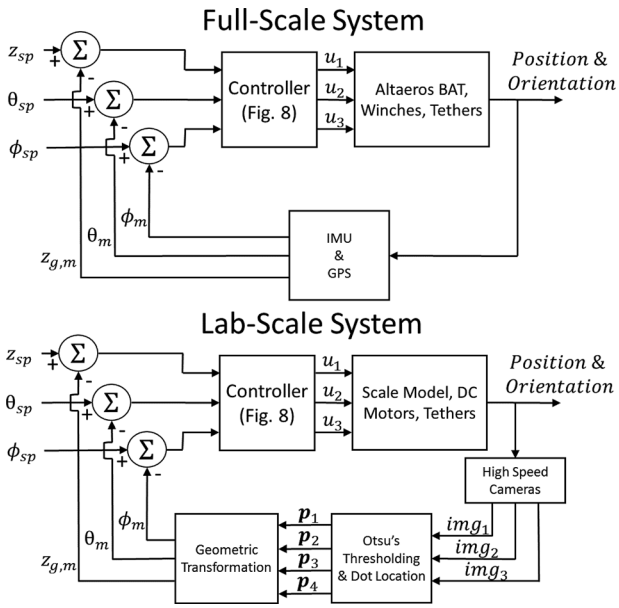

Fig. 7 Comparison of the control structure of lab-scale and full-scale system. The new, enhanced motion capture and image processing algorithms detailed in this paper are located in the feedback loop of the lab-scale system. While the plant and feedback instrumentation differ between setups, the controller does not. The variable, $\mathbf{p}_i$, is a matrix containing four scalars, the *x* and *y* pixel coordinates of each set of dots within the image img_i. This is explained in detail in Sec. 3.1.

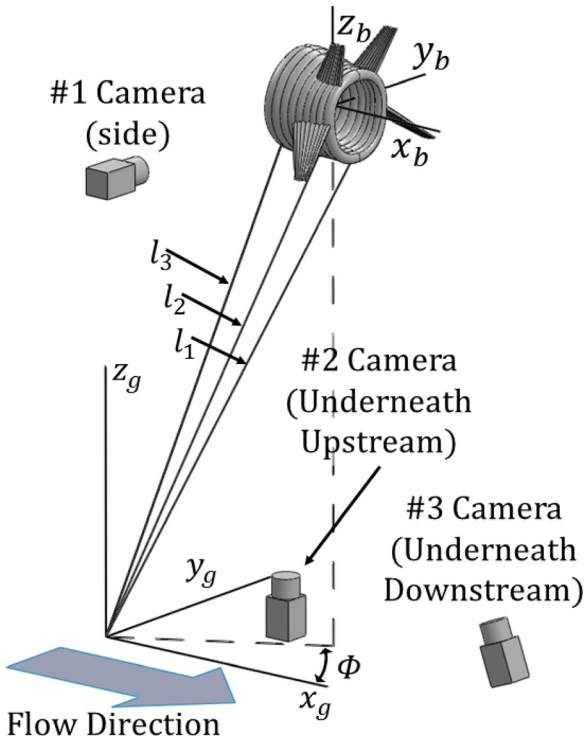

Fig. 8 Schematic depiction of three-tether AWE system based on the Altaeros BAT with zero roll, pitch, and yaw, including camera locations, tether lengths (l_i), and azimuth angle (Φ)

coordinate system at the models center of mass. The model orientation (attitude) is characterized through roll (ϕ), pitch (θ), and yaw (ψ) Euler angles.

In order to design a controller capable of producing crosswind flight, it is necessary to resolve the position and orientation of the model in real time. A schematic representing the system is shown in Fig. 8. It shows the ground-fixed coordinate system, denoted by the subscript "g," as well as the body-fixed coordinate system, denoted by the subscript "b." All of the key variables used in this work are summarized in Table 1.

The unit vectors representing the body fixed x, y, and z axes are represented as three-component vectors in the ground-fixed system. Figure 8 also shows the lengths of the center tether, l_1, starboard tether, l_2, and port tether, l_3.

In characterizing a crosswind flight trajectory, it will be convenient to examine the azimuth angle, which is shown in Figs. 3 and 8 and is defined as

$$\Phi = \arctan\frac{y_g}{x_g} \tag{16}$$

Table 1 Relevant variables and descriptions

Variable	Description	Units
$\mathbf{r}$	Position of model	cm
$\mathbf{v}$	Velocity of model	$\mathrm{cm}\cdot\mathrm{s}^{-1}$
$\mathbf{v}_f$	Free stream flow velocity	$\mathrm{cm}\cdot\mathrm{s}^{-1}$
$\mathbf{v}_a$	Velocity of apparent wind	$\mathrm{cm}\cdot\mathrm{s}^{-1}$
Φ	Azimuth angle	—
Λ	Zenith angle	—
ϕ, θ, ψ	Roll, pitch, and yaw angles	—
$\hat{x}_b, \hat{y}_b, \hat{z}_b$	Unit vectors of body-fixed coordinate system	cm
l_1, l_2, l_3	Center, starboard, and port tether lengths	cm
$\mathbf{r}_1, \mathbf{r}_2, \mathbf{r}_3$	Camera #1, #2, and #3 positions in ground-fixed coordinates	cm
u_1, u_2, u_3	Commanded tether release speeds	$\mathrm{cm}\cdot\mathrm{s}^{-1}$

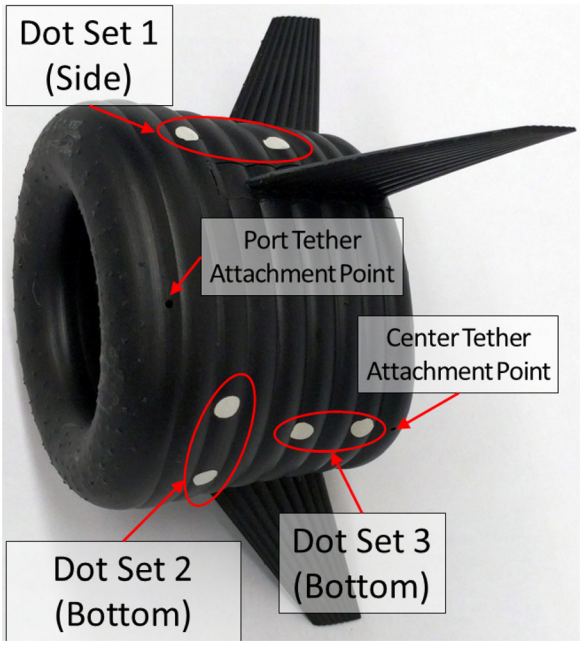

Fig. 9 Image of 3D printed, 1:100 scale model of the Altaeros BAT (approximately 8 cm in length), showing image tracking dot sets as well as two of the three tether attachment points. The starboard tether attachment point is not visible in the image.

The azimuth angle characterizes the extent by which the lifting body deviates from a direct downwind configuration. Under successful crosswind flight, Φ will exhibit periodic oscillations about $\Phi = 0$.

3.1 Motion Capture System. Successful crosswind flight in the lab-scale setup requires continuous, accurate measurements of the lifting body's position and orientation (attitude). This means that the three cameras depicted in Fig. 8 must continually track the white dots on the model, as shown in Fig. 9. A basic threshold-based image processing algorithm was implemented in the previous work [22], for accomplishing this on a stationary AWE system; however, successful motion capture for crosswind flight places increasing demands on the underlying image processing algorithms, as they must track a fast-moving system under varying lighting conditions. The enhanced system has augmented the effective field of view and increased the degree of dynamic behavior that can be accurately tracked. This subsection details the enhanced motion capture system that has been implemented for these purposes, which consists of two key steps:

(1) Dot centroid detection in a single still frame.
(2) Derivation of AWE position and orientation from dot centroid locations.

The location of this improved motion capture algorithm within the overall control scheme is shown in the feedback loop of the lab-scale system in Fig. 7.

3.1.1 Dot Centroid Detection. The first step in resolving the position and orientation of the model is to locate the visual targets (white dots) in each of the source images. To decrease processing time, a small region of interest (ROI) is first extracted from the source image for each camera. This ROI matrix $\mathbf{G}$ is a two-dimensional matrix of gray-scale values ranging from 0 to 255. To classify each pixel in the ROI as belonging to a dot or the background, a threshold-based technique known as *Otsu's method* [25] is used. This method works by generating an intensity histogram from the ROI matrix and then calculating the intra-class variance, σ_w^2 for each intensity value ξ. The intra-class variance is defined in the following equation:

$$\sigma_w^2(\xi) = \omega_L^2(\xi)\sigma_L^2(\xi) + \omega_R^2(\xi)\sigma_R^2(\xi) \tag{17}$$

Here, ω_L is the weighted probability of the class to the left of the point being considered on the histogram and ω_R is the weighted probability of the class on the right of the point being considered on the histogram. Variances appear in Eq. (17) as σ_L^2 and σ_R^2. These represent the variance of the left and right classes, respectively. It is shown in Ref. [25] that the value ξ_0 that minimizes σ_w^2

$$\xi_0 = \arg \min_{\xi'} \{\sigma_w^2(\xi')\} \tag{18}$$

is an accurate approximation of the best threshold level. Based on ξ_0, all pixels in the ROI are classified as 1 or 0 in a binary matrix, $\mathbf{B}$, whose entries are specified as follows:

$$\mathbf{B}_{ij} = \begin{cases} 1, & \mathbf{G}_{ij} \geq \xi_0 \\ 0, & \text{otherwise} \end{cases} \tag{19}$$

The binary matrix is divided either horizontally or vertically (depending on which camera and ROI is being considered) into two smaller matrices, $\mathbf{B}_1 \in \mathbb{R}^{m_1 \times n_1}$ and $\mathbf{B}_2 \in \mathbb{R}^{m_2 \times n_2}$. The precise dividing line between the two matrices is based on the horizontal or vertical centroid location of $\mathbf{B}$ (horizontal if the matrix is divided horizontally; vertical if the matrix is divided vertically). Once $\mathbf{B}_1$ and $\mathbf{B}_2$ have been obtained, coordinates of the dot centers, denoted by x_{c1}, y_{c1}, x_{c2}, and y_{c2}, are located by calculating individual components of a discrete two-dimensional geometric centroid according to the following equation:

$$\begin{aligned} x_{c1} &= \frac{\sum_{i=0}^{m_1}\sum_{j=0}^{n_1} j b_{1ij}}{\sum_{i=0}^{m_1}\sum_{j=0}^{n_1} b_{1ij}}, \quad y_{c1} = \frac{\sum_{i=0}^{m_1}\sum_{j=0}^{n_1} i b_{1ij}}{\sum_{i=0}^{m_1}\sum_{j=0}^{n_1} b_{1ij}} \\ x_{c2} &= \frac{\sum_{i=0}^{m_2}\sum_{j=0}^{n_2} j b_{2ij}}{\sum_{i=0}^{m_2}\sum_{j=0}^{n_2} b_{2ij}}, \quad y_{c2} = \frac{\sum_{i=0}^{m_2}\sum_{j=0}^{n_2} i b_{2ij}}{\sum_{i=0}^{m_2}\sum_{j=0}^{n_2} b_{2ij}} \end{aligned} \tag{20}$$

Here, b_{1ij} is the component located in the ith row and the jth column of the first binary matrix, $\mathbf{B}_1$, and b_{2ij} is the component located in the ith row and the jth column of the second binary matrix, $\mathbf{B}_2$. The individual position components are then transformed back into coordinates in the original image by simple addition with the position coordinates of the ROI within the overall image.

This procedure is performed four times on three different source images at every time-step. As depicted in Fig. 8, camera #2 tracks dot sets 2 and 3, which are located on the bottom of the model, as shown in Fig. 9. Camera #1 tracks dot set #1, which is located on the side of the model, and camera #3 tracks only dot set # 3. This produces four vectors $\mathbf{p}_i \in \mathbb{R}^4$ given by

$$\mathbf{p}_i = [x_{c1}^i \quad y_{c1}^i \quad x_{c2}^i \quad y_{c2}^i] \tag{21}$$

where the index $i \in \{1, 2, 3, 4\}$ specifies the combination of camera and dots being tracked.

3.1.2 Derivation of Orientation and Position. Each set of dots is aligned with either the body-fixed x or y axis; specifically, two of the ROIs track dots oriented along the x_b axis, whereas the other two track dots that are oriented along the y_b axis. Table 2 delineates the precise geometric information that is provided by each camera and each set of dots. This information is sufficient

Table 2 Resolution of specific body-fixed unit vector components

Unit vector	Component	Camera	Dot set
$\hat{x}_b$	x_g	1	1
$\hat{x}_b$	y_g	2	3
$\hat{x}_b$	z_g	1	1
$\hat{y}_b$	x_g	2	2
$\hat{y}_b$	y_g	2	2
$\hat{y}_b$	z_g	3	2

for the calculation of the unit vectors $\hat{x}_b$ and $\hat{y}_b$ in ground-fixed coordinates. Once $\hat{x}_b$ and $\hat{y}_b$ have been determined, $\hat{z}_b$ is determined from a simple cross product; specifically, $\hat{z}_b = \hat{x}_b \times \hat{y}_b$. The complete set of body-fixed unit vectors in the ground-fixed coordinate system forms the columns of a rotation matrix that encodes the Euler angles, namely, roll (ϕ), pitch (θ), and yaw (ψ).

Because the position of the model is necessary to determine the conversion factor between pixels and distance, and because position is required for dynamic characterization and flight control, $\mathbf{r}$ is also computed at each time-step. This is accomplished by using the location of each group of dots in each frame to provide a measurement relative to the centerline of the camera view. The individual components of the position vector $\mathbf{r}$ satisfy the system of equations given by the following equation:

$$\begin{aligned} r_x &= r_{2,x} - \left(\frac{N_V}{2} - v_{\text{dots},2}\right)(|\mathbf{r}_2 - \mathbf{r}|)\left(\frac{2\tan\gamma}{N_V}\right) \\ r_y &= r_{2,y} + \left(\frac{N_H}{2} - h_{\text{dots},2}\right)(|\mathbf{r}_2 - \mathbf{r}|)\left(\frac{2\tan\gamma}{N_H}\right) \\ r_z &= r_{1,z} - \left(\frac{N_V}{2} - v_{\text{dots},1}\right)(|\mathbf{r}_1 - \mathbf{r}|)\left(\frac{2\tan\gamma}{N_V}\right) \end{aligned} \tag{22}$$

where $r_{2,x}$ is the x component of the bottom, upstream camera position vector, $r_{2,y}$ is the y component of the bottom upstream camera position vector, and $r_{1,z}$ is the z component of the side camera position vector. Furthermore, N_H and N_V are the number of horizontal and vertical pixels in an image, and γ is the view angle of the camera relative to the centerline. The position of the dots within each frame is denoted as $v_{\text{dots},1}$ for the vertical position of the dots in the frame from the bottom upstream camera, $h_{\text{dots},2}$ for the horizontal position of the dots in the frame from the bottom upstream camera, and $v_{\text{dots},1}$ for the vertical position of the dots in the frame from the front camera. Note that the vertical position in the frame is measured from the top of the image down.

Because this system relies on digital images, it produces quantization error. In general, the magnitude of this error will be a nonlinear function of the true position and orientation. However, it is possible to provide an estimate of the typical (average) value of this error, which will not vary by more than approximately 10% over the course of flight. Typically, the total distance between dot centers in an image is image approximately 80 pixels. Therefore, the quantization error in orientation, calculated through a simple arc tangent, is approximately 0.7 deg. The quantization error in position can be approximated by using the derivative of Eq. (22) with respect to $\mathbf{r}$. For a set of dots in the middle of the camera field of view, and the center of the water channel, it is found to be approximately 1 mm.

4 Dynamic Scaling Analysis for Lab-Scale/Full-Scale Equivalence

In order to compare the closed-loop dynamic behavior across model scales, we utilize the Buckingham-Pi theorem of Ref. [26] to derive relationships that describe how to appropriately scale plant and controller parameters. Although the dynamic model detailed in Eqs. (1)–(6) does not provide the level of detail that actual flight tests provide (hence the desire for an experimental setup), it does provide enough information to identify key variables in the system dynamics which is essential for applying the Buckingham-Pi theorem. This section first reviews the methods and results of Ref. [23], which are used to scale the *plant*. Then, we derive a new set of scaling laws that describe how the controller of the lab-scale system should be scaled to achieve dynamic equivalence. Together, these two sets of scaling laws provide a set of guidelines for achieving dynamic similarity between the lab-scale and full-scale systems under closed-loop control.

Table 3 Physical dependencies used to describe the characteristics of the lifting body as identified from the dynamic model

Parameter	Variable	Units
Mean tether length	L_t	m
Aerodynamic chord length	L_c	m
Tether diameter	d_t	m
Mass of aerostat	M_a	kg
Fluid density	ρ	$\text{kg}\cdot\text{m}^{-3}$
Wind or flow speed	v_f	$\text{m}\cdot\text{s}^{-1}$
Gravitational acceleration	g	$\text{m}\cdot\text{s}^{-2}$
Azimuth rate of change	$\dot{\Phi}$	s^{-1}
Azimuth acceleration	$\ddot{\Phi}$	s^{-2}
Zenith rate of change	$\dot{\Lambda}$	s^{-1}
Zenith angle acceleration	$\ddot{\Lambda}$	s^{-2}
Tether twist angle rate of change	$\dot{\Psi}$	s^{-1}
Tether twist acceleration	$\ddot{\Psi}$	s^{-2}
Linear tether density	λ	$\text{kg}\cdot\text{m}^{-1}$

4.1 Dynamic Scaling Analysis of Plant Parameters.

Starting with the dynamic model detailed previously, Ref. [22] identifies several key plant parameters. For completeness, these results are summarized here. A list of key dimensional plant parameters identified from the dynamic model are detailed in Table 3. Using the Buckingham-Pi theorem [26], these parameters are then related to each other via the set of nondimensional groups

$$\left\{\frac{L_c}{L_t}, \frac{L_t}{d_t}, \frac{L_t^3\rho}{M_a}, \frac{\lambda L_t}{M_a}, \frac{gL_t}{V^2}, \frac{L_t\dot{\Phi}}{V}, \frac{L_t^2\ddot{\Phi}}{V^2}, \frac{L_t\dot{\Lambda}}{V}, \frac{L_t^2\ddot{\Lambda}}{V^2}, \frac{L_t\dot{\Psi}}{V}, \frac{L_t^2\ddot{\Psi}}{V^2}\right\} \tag{23}$$

which must remain constant across model scales in order to ensure dynamic similarity. However, in these dimensionless groups, there is a direct variation of the velocity and length scales, thus rendering it impossible to vary both flow speed and length scale while simultaneously maintaining dynamic equivalence according to the sixth through eleventh dimensionless variables in Eq. (23). This contradiction can be resolved by introducing a normalized time, $\bar{t}$, which is related to absolute time, (t), through a scalar parameter, α

$$\bar{t} = \alpha t, \quad \alpha \propto \frac{1}{\sqrt{L_c}} \tag{24}$$

This relationship reflects uniformly altered time constants (altered through the "stretching" factor, α), at small scale versus full-scale. The new dimensionless groups, where derivatives are calculated relative to the normalized time, $\bar{t}$, are

$$\left\{\frac{L_c}{L_t}, \frac{L_t}{d_t}, \frac{L_t^3\rho}{M_a}, \frac{\lambda L_t}{M_a}, \frac{\bar{g}L_t}{\bar{V}^2}, L_t\frac{d\Phi}{d\bar{t}}\bar{V}, \frac{L_t^2\dfrac{d^2\Phi}{d\bar{t}^2}}{\bar{V}^2}, L_t\frac{d\Lambda}{d\bar{t}}\bar{V}, \frac{L_t^2\dfrac{d^2\Lambda}{d\bar{t}^2}}{\bar{V}^2}, L_t\frac{d\Psi}{d\bar{t}}\bar{V}, \frac{L_t^2\dfrac{d^2\Psi}{d\bar{t}^2}}{\bar{V}^2}, \bar{t}\right\} \tag{25}$$

Table 4 Controller parameters that impact dynamic behavior of crosswind flight

Parameter	Variable	Units
Roll controller proportional gain	$k_{p\phi}$	$m \cdot s^{-1}$
Pitch controller proportional gain	$k_{p\theta}$	$m \cdot s^{-1}$
Altitude controller proportional gain	k_{pz}	s^{-1}
Roll controller derivative gain	$k_{d\phi}$	m
Pitch controller derivative gain	$k_{d\theta}$	m
Altitude controller derivative gain	k_{dz}	—
Roll controller time constant	τ_ϕ	s
Pitch controller filter time constant	τ_θ	s
Altitude controller filter time constant	τ_z	s
Pitch setpoint	θ_{SP}	—
Altitude setpoint	Z_{SP}	m
Roll setpoint amplitude	a_0	—
Roll setpoint period	T	s
Tether release/retract speed limit	v_l^{sat}	$m \cdot s^{-1}$

These dimensionless groups lead to the following guidelines for achieving dynamic similarity:

(1) Individual tether lengths l_1, l_2, and l_3 must be scaled by the same factor as the model length, thereby maintaining geometric similarity.
(2) Net buoyancy (F_{bouyant}/mg) must be preserved at lab-scale and full scale.
(3) Taking L as the length-scale factor (i.e., a 1:100-scale model would have $L = (1/100)$), flow speed should be scaled according to the *square root* of L, i.e., $v_f \propto \sqrt{L} v_{\text{full}}$, where v_{full} is the target velocity of the full-scale system for which we wish to replicate flight characteristics. This scaling rule ensures preservation of the fifth dimensionless group (the inverse of the Froude number squared) at scale.

These scaling rules are valid under two assumptions:

(1) Mass distribution is identical at lab-scale and full-scale, which means that the moments of inertia are completely determined by the mass and scale factor, L. This assumption is satisfied through proper design of 3D printed models.
(2) Aerodynamic coefficients are independent of the Reynolds number within the Reynolds number ranges seen in the water channel (75,000 at a 1 m/s flow speed, using chord length as the reference length) and full-scale system (5,000,000 at a 10 m/s wind speed). Hence, the viscosity of the medium is neglected as a physical dependency. The approximate validity of this assumption has been verified experimentally in Ref. [23] for the Altaeros BAT.

4.2 Dynamic Scaling Analysis of Controller Parameters. In order to compare dynamic behavior under closed-loop control across model scales, it is necessary to extend the dimensional analysis of Ref. [23] to include controller parameters. From the controller detailed in Eq. (10) and Fig. 4, we identify the gains, time constants, and setpoints of the controllers as the relevant parameters. A detailed explanation of each parameter, along with associated units, is provided in Table 4.

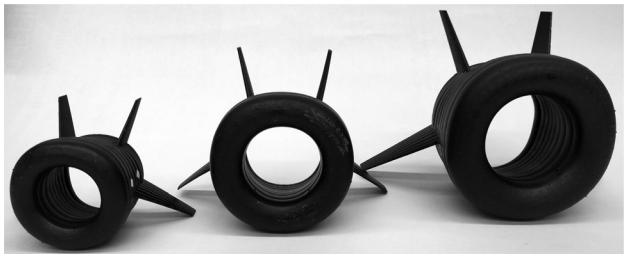

Fig. 10 Three different scale models of the Altaeros BAT. The smallest (left) has a characteristic length that is 75% of the characteristic length of the 1:100 model (middle). The largest (right) has a characteristic length that is 125% of the characteristic length of the 1:100 model (middle).

The next step in Buckingham-Pi analysis is to derive dimensionless groups. Since k_{dz}, θ_{SP}, and a_0 are already dimensionless, they can be removed from the analysis, and the resulting analysis produces 11 dimensionless groups

$$\left\{\frac{L_c}{Z_{SP}}, \frac{L_c}{k_{d\theta}}, \frac{L_c}{k_{d\phi}}, tk_{pz}, \frac{v_f}{k_{p\theta}}, \frac{v_f}{k_{p\phi}}, \frac{v_f}{v_l^{\text{sat}}}, \frac{t}{\tau_z}, \frac{t}{\tau_\theta}, \frac{t}{\tau_\phi}, \frac{t}{T}\right\} \tag{26}$$

Given the analysis results of Eqs. (24) and (25) in Sec. 4.1, which demonstrate that time (and all time constants) scale according to $t \propto \sqrt{L_c}$, along with the results of Eq. (26), we arrive at the following scaling laws:

(1) Scale the derivative gains of the roll and pitch controllers, $k_{d\theta}$ and $k_{d\phi}$, according to the length scale, L_c.
(2) Scale the proportional gains of the roll and pitch controllers, $k_{p\theta}$ and $k_{p\phi}$, along with the tether speed saturation limit, v_l^{sat} according to $\sqrt{L_c}$.
(3) Scale the proportional gain of the altitude controller, k_{pz}, according to $(1/\sqrt{L_C})$.
(4) Scale the filter time constants, $\tau_{z,\theta,\phi}$ as well as the roll setpoint period, T, according to $\sqrt{L_c}$.

Under the aforementioned scaling laws for both the plant and the controller, the full-scale dynamic behavior will be replicated at lab scale with the only exception being uniformly accelerated time constants. In particular, the lab-scale time constants will scale uniformly according to the square root of the length scale, i.e., $\tau \propto \sqrt{L_c}$, where τ represents any system time constant (Table 5).

5 Experimental Validation Results and Discussion

To experimentally evaluate crosswind flight and dynamic similarity at different scales, we consider three different scale models, as shown in Fig. 10, rather than comparing a single lab-scale model to a full-scale model (which we have very limited access to and no means of controlling the experiment, since wind is random). These models are termed the small, medium, and large models. The small-scale model has a chord length, L_c^s, equal to

Table 5 Relationship of experiments for the small, medium, and large models at two different flow speeds

Model size	Flow speed, v_f (cm/s)	Normalized flow speed, $\bar{v}_f$ (cm/s)	Flow speed index	Roll setpoint period range (s)	Normalized roll setpoint period range (s)
Small	22.0	25.4	A	4.330–7.578	5.000–8.750
Medium	25.0	25.0	A	6.000–8.750	6.000–8.750
Large	28.0	25.0	A	6.708–10.90	6.000–9.750
Small	16.5	19.1	B	4.330–6.495	5.000–7.500
Medium	18.8	18.8	B	4.500–8.500	4.500–8.500
Large	21.0	18.8	B	6.708–9.783	6.000–8.750

Table 6 Variance (with respect to the mean curve) for data presented in Figs. 11–13

Model size	Normalized	Roll angle variance (rad^2)	Yaw angle variance (rad^2)	Azimuth angle variance (rad^2)
Small	No	0.0209	0.0309	0.0756
Small	Yes	0.00949	0.00463	0.0141
Medium	No	0.0221	0.0365	0.0971
Medium	Yes	0.00533	0.00809	0.0207
Large	No	0.0228	0.0287	0.108
Large	Yes	0.00913	0.00903	0.0462

75% of the chord length of the medium-scale model, L_c^m, and the large-scale model has a chord length, L_c^l, equal to 125% of the medium-scale model. The medium model is a 1:100 scale model of the 2013 Altaeros BAT prototype. The largest of these models presents a blockage ratio of approximately 1.5% in the UNC Charlotte water channel.

Each of the three scale models was subjected to the crosswind flight control algorithm of Sec. 2.3 at two different flow speeds, for a duration of at least 20 periods corresponding to between 90 s and 210 s depending on the roll setpoint period being tested. This was found to be sufficient for the mean power ratio to converge. At both normalized flow speeds, each model was subjected to between 11 and 18 experiments wherein some experiments were run multiple times to ensure consistency. Periods were chosen to provide a normalized period resolution of 0.25 s. The organization of individual experiments is shown in Table 6. Note that the exact matching of normalized flow speeds is limited by quantization of the flow speed measurement, which is discussed in detail in Sec. 5.4.

The results presented in this section have three purposes:

(1) To demonstrate successful crosswind flight at many different operating conditions and model scales.
(2) To validate previously derived dynamic scaling laws for the controller parameters.
(3) To demonstrate an increase in power production potential from crosswind flight, quantified by the power ratio of Eq. (13).

5.1 Dynamic Scaling of Controller for Experiments. In order to compare between models, we relate the normalized time, $\bar{t}$, of the large and small models to the normalized time of the medium model using the relationship provided in Ref. [23]. Specifically, $\bar{t} = \alpha t$, where $\alpha \propto \sqrt{L_c}$. Normalized times are calculated as

$$\bar{t}^s = \alpha^s t, \quad \bar{t}^m = \alpha^m t, \quad \bar{t}^l = \alpha^l t \tag{27}$$

For the chosen model scales, this resulted in

$$\alpha^s = 1.15 s^{-1}, \quad \alpha^m = 1 s^{-1}, \quad \alpha^l = 0.894 s^{-1} \tag{28}$$

During the course of a single experiment, the controller for each model was held constant. It was then varied across model scales according to the scaling laws derived in Sec. 4.2, using the scale factors of Eq. (28). The exact values used for controller parameters are given in Table 7.

5.2 Comparison of Time-Dependent Quantities. In order to compare individual quantities such as roll, yaw, or azimuth under crosswind flight, it is also necessary for the normalized period of the roll setpoint to be the same across all three model scales. By characterizing each model over the same range of *normalized* crosswind periods, we are able to compare the dynamic behavior during crosswind flight across all three model scales. An example of this comparison for a single normalized roll setpoint period is shown in Figs. 11–13. For each of the curves in Figs. 11–13, the average of the three curves was calculated, and the mean squared error from this averaged was subsequently calculated, in order to provide a signal variance that quantified the closeness of the curve to the mean. The signal variances for each of the experiments are reported in Table 6. These results demonstrate that the

Table 7 Constant controller parameters for the small, medium, and large models as related through dynamic scaling laws

Parameter	Value–small model	Value–medium model	Value–large model
$k_{p\phi}$	8.66	10.0	11.18
$k_{p\theta}$	4.33	5.00	5.59
k_{pz}	0.115	0.10	0.089
$k_{d\phi}$	2.25	3.00	3.75
$k_{d\theta}$	0.75	1.00	1.25
k_{dz}	0.00	0.00	0.00
τ_ϕ	0.13	0.15	0.168
τ_θ	0.173	0.20	0.224
τ_z	0.217	0.250	0.280
θ_{sp}	5.00	5.00	5.00
z_{sp}	45.0	60.0	75.0
a_0	15.0	15.0	15.0
v_l^{sat}	0.0677	0.0606	0.0524

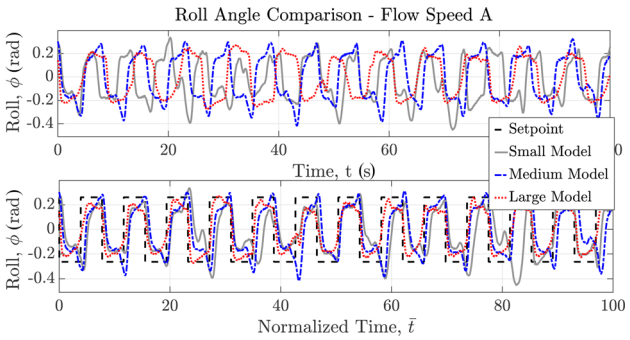

Fig. 11 Comparison of controlled roll angle plotted against time, *t* (top), and normalized time, $\bar{t}$ (bottom)

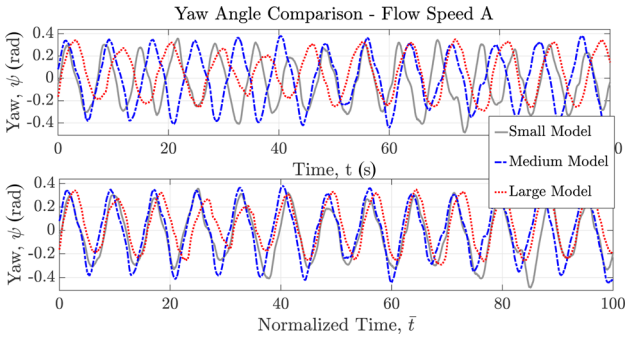

Fig. 12 Comparison of uncontrolled yaw angle plotted against time, *t* (top), and normalized time, $\bar{t}$ (bottom)

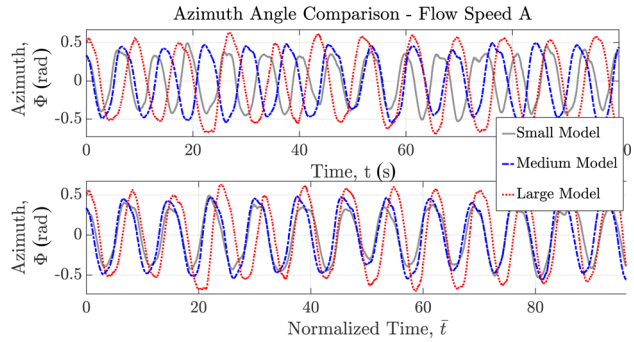

Fig. 13 Comparison of uncontrolled azimuth angle plotted against time, t (top) and normalized time, $\bar{t}$ (bottom)

time-dependent, nondimensional quantities of roll angle, heading (yaw angle), and azimuth angle exhibit very similar amplitudes, phase shifts, frequencies, and nondimensionalized transient response characteristics across all scales.

5.3 Comparison of Aggregate Quantities. Mean power ratio, $\bar{P}$, was measured for each of several roll setpoint periods, for flow speeds A and B, using Eq. (13). This means power ratio is given by

$$\bar{P}(T_i) = \frac{1}{t_f - t_0}\int_{t_o}^{t_f} P(t, T_i)dt \tag{29}$$

where the instantaneous power ratio, $P(t, T_i)$, is given by Eq. (13). For this analysis, we took $C_p = 0.5$, $\eta_m = 0.9$, $\eta_g = 0.75$, $A^s_{\text{ref}} = 11\,\text{cm}^2$, $A^m_{\text{ref}} = 20\,\text{cm}^2$, and $A^l_{\text{ref}} = 31\,\text{cm}^2$. Because we did not have direct measurements of individual tether tensions, and because estimating tether tension from a model-based method such as finite element analysis is a challenging and complex problem outside the scope of this work, it is necessary to approximate the individual tether tensions in Eq. (13) through a simple, quasi-static model based on known fluid dynamic and buoyancy characteristics of the system (which drive the tensions). Specifically, we approximated individual tether tensions by

$$\tau_i(t) = \frac{1}{3}\left(F_L(\theta)\cos(\Lambda - \theta) + F_D(\theta)\sin(\Lambda - \theta) + F_b\cos(\Lambda)\right) \tag{30}$$

where F_b represents the net buoyant force. The net lift and drag forces, F_L and F_D, were estimated based on known characterizations of the lifting body. It is important to note that this method contains many simplifying assumptions, and therefore, should be considered as a coarse estimate for the purpose of illustration. Nonetheless, for the results shown here, the magnitude of the control power calculated via Eq. (30) rarely exceeded 5% of the power generated or about 25% of the excess power created through crosswind flight.

A curve was then fit to the data for $\bar{P}$ as a function of the crosswind period, T, using an exponentially weighted regression function. An example form of this function for the small model at flow speed A is given by

$$\hat{P}^s_A(T|\mathbb{T}^s_A, \mathbb{P}^s_A) = \sum_{i=1}^{\eta} w(T|\mathbb{T}^s_A)\bar{P}^s_{i,A} \tag{31}$$

where $\mathbb{T}^s_A = \{T^s_{1,A}, T^s_{2,A}, \ldots, T^s_{\eta,A}\}$ is the set of all roll setpoint periods tested for flow speed A, $\mathbb{P}^s_A = \{\bar{P}^s_{1,A}, \bar{P}^s_{2,A}, \ldots, \bar{P}^s_{\eta,A}\}$ is the set of corresponding measured mean power ratios given by Eq. (13), and $\eta \in \mathbb{N}$ is the number of periods tested for the small model at flow speed A. The individual weight for a particular roll setpoint period, T, $w(T|\mathbb{T}^s_A)$, is given by

$$w(T|\mathbb{T}^s_A) = \frac{e^{-c\left(T - T^s_{i,A}\right)^2}}{\sum_{i=1}^{\eta} e^{-c\left(T - T^s_{i,A}\right)^2}} \tag{32}$$

where c is a tuning parameter, chosen to be 5 s^{-2} in this work. Equivalent equations for the best curve for the medium and large models at specific flow speeds are given by changing the superscript s to m or l and the subscript A to B as appropriate. The raw data, along with the fit curves, are shown for both the mean power factor and 85 percentile power factor in Fig. 14.

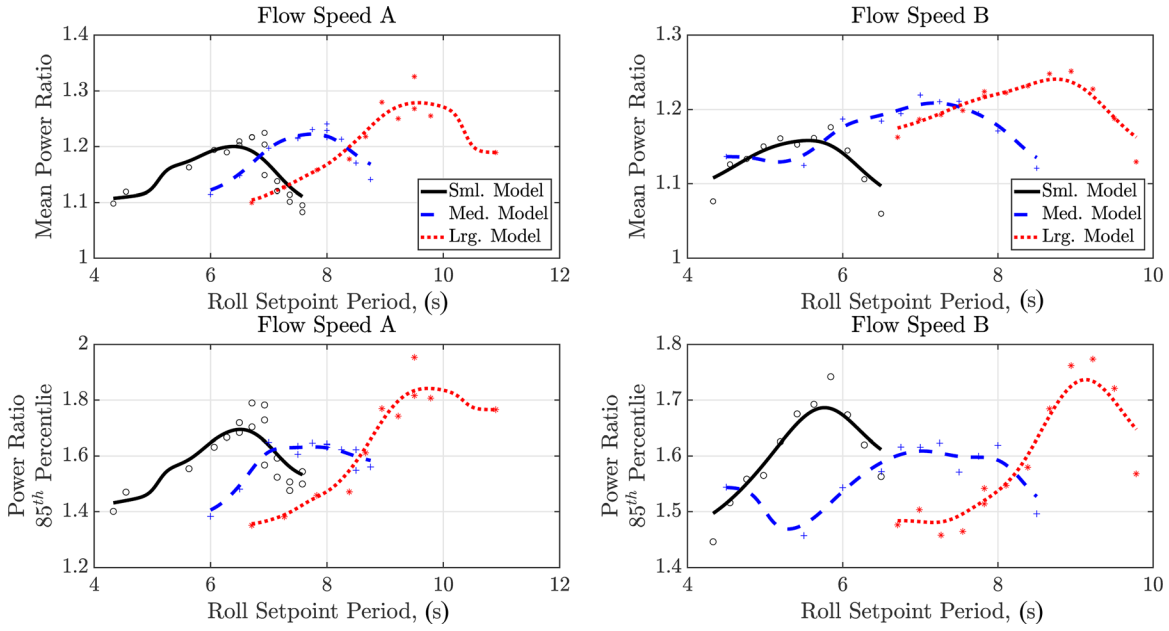

Fig. 14 The top plots shows the measured mean power ratios, $\mathbb{P}^s_{A,B}$, $\mathbb{P}^m_{A,B}$, or $\mathbb{P}^l_{A,B}$ plotted against the corresponding set of roll setpoint periods $\mathbb{T}^s_{A,B}$, $\mathbb{T}^m_{A,B}$, or $\mathbb{T}^l_{A,B}$ along with their associated best fit curves given by Eqs. (31) and (32). The bottom plot shows the same for the power ratio 85th percentile.

Table 8 Predicted and measured scale factors, slow flow speed

Model size	Flow speed	Predicted scale factor, α	Experimentally identified scale factor, $\hat{\alpha}$	Error (%)
Small	B	1.15	1.30	13
Large	B	0.894	0.846	5.4
Small	A	1.15	1.22	6.7
Large	A	0.894	0.806	10

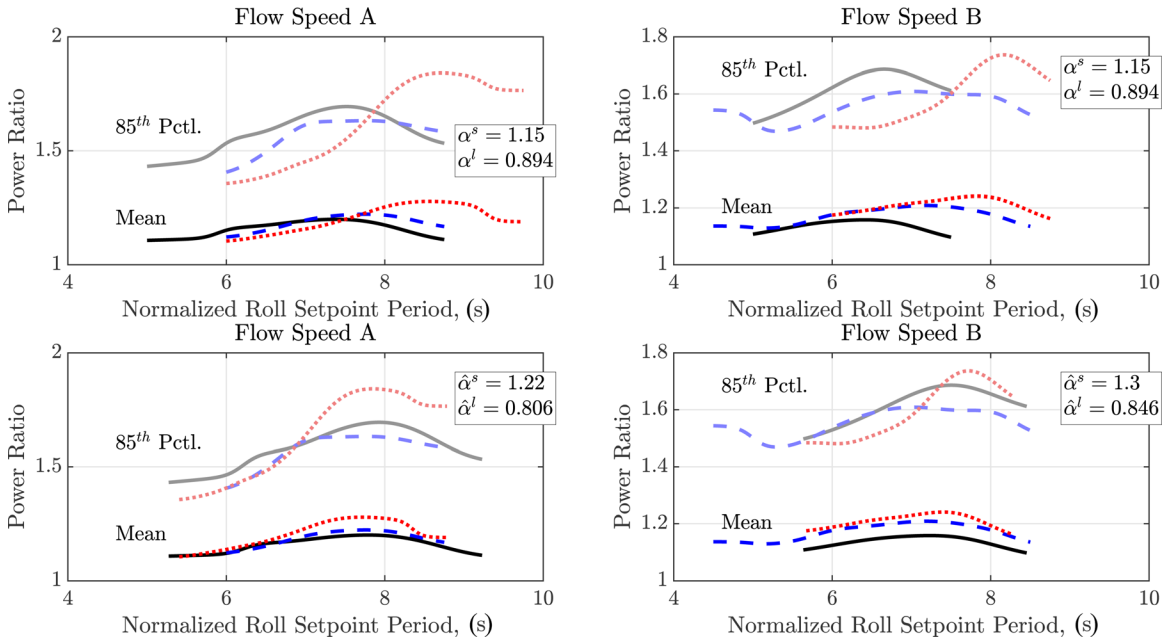

Fig. 15 The top plot shows the power ratio plotted against the normalized roll setpoint period calculated from nominal time scale factors, α^s, α^m, and α^l. The bottom plot shows the mean power ratio plotted against the normalized roll setpoint period calculated by using the scale factors $\hat{\alpha}^s$ and $\hat{\alpha}^l$ given by Eq. (33).

The experimentally identified scale factors for the small and large models, relative to the medium model, $\hat{\alpha}^s$ and $\hat{\alpha}^l$, were then calculated as the scale factors that resulted in the best fit between the power ratio curve of the small or large model and power ratio curve of the medium model, as given by Eqs. (31) and (32). Specifically, $\hat{\alpha}^s$ and $\hat{\alpha}^l$ were calculated as the scale factors that minimized the root-mean-square error in between the power ratio regression of the large or small model and the power ratio regression of the medium model. For example, the expression for the small model at flow speed A reads

$$\hat{\alpha}^s = \arg\min_{\tilde{\alpha}^s}\left\{\frac{1}{T_f - T_0}\int_{T_0}^{T_f} \|\hat{P}^s\left(T|\tilde{\mathbb{T}}_A^s, \mathbb{P}_A^s\right) - \hat{P}^m\left(T|\bar{\mathbb{T}}_A^m, \mathbb{P}_A^m\right)\| dT\right\} \tag{33}$$

where $\tilde{\mathbb{T}}_A^s = \{\tilde{\alpha}^s T_{1,A}^s, \tilde{\alpha}^s T_{2,A}^s, \ldots, \tilde{\alpha}^s T_{\eta,A}^s\}$ denotes the set of all normalized roll setpoint periods for the small model at flow speed A calculated using the variable scale factor $\tilde{\alpha}^s$, and $\bar{\mathbb{T}}_A^m = \{\alpha^m T_{1,A}^s, \alpha^m T_{2,A}^s, \ldots, \alpha^m T_{\eta,A}^s\}$ denotes the set of all normalized roll setpoint periods for the medium model at flow speed A calculated using the nominal scale factor α^m calculated directly from the length scale, given in Eqs. (27) and (28). Note that since $\alpha^m = 1$, $\bar{\mathbb{T}}_j^m = \mathbb{T}_j^m \quad \forall j \in \{A, B\}$.

The limits on the integral of Eq. (33) bound the region where the curve fits overlap and will also depend on $\tilde{\alpha}^s$. Specifically

$$T_0 = \max\{\min\{\tilde{\mathbb{T}}_A^s\}, \min\{\bar{\mathbb{T}}_A^m\}\} \tag{34}$$

$$T_f = \min\{\max\{\tilde{\mathbb{T}}_A^s\}, \max\{\bar{\mathbb{T}}_A^m\}\} \tag{35}$$

Plots of the best fit curve for the mean power factor of the small, medium, and large models are shown by the darker curves in Fig. 14. The average power ratio is limited by frequent tacking, which arises due to tether length limitations in the water channel. In fact, the bottom plots of Fig. 14 show the 85th percentile power ratio, demonstrating that the system indeed achieves power ratios close to two over substantial portions of the crosswind motion. Maximizing the fraction of crosswind flight over which these larger power ratios are realized represents an important topic of ongoing control design research.

We compare the measured scale factors, given by Eq. (33), $\hat{\alpha}^s$ and $\hat{\alpha}^l$ to the predicted values, α^s and α^l, calculated directly from the characteristic lengths in Table 8. Figure 15 shows plots of the power ratio as a function of the normalized roll setpoint period, as calculated using both the predicted and measured scale factors.

5.4 Discussion and Error Analysis. Because the roll angle is controlled to a setpoint that is scaled according to the known characteristic lengths of the models, it is expected that the roll signals will overlap well when the horizontal axis of Fig. 11 is normalized using nominal scaling. Similarly, it is unsurprising that the yaw and azimuth angles exhibit the same normalized frequencies

across different scales. The most significant result is the similarity in *amplitude* and general transient response characteristics of the uncontrolled signals, yaw, and azimuth. Because these quantities are nondimensional, their magnitudes should be independent of the model scale. This in fact conforms to the result shown in Figs. 12 and 13.

The dynamic scaling laws derived in this work and Ref. [23] are valid under the condition that *all* variables appearing the dimensionless groups are scaled precisely. If any of these variables is not scaled precisely, it can undermine the accuracy of the results. In this work, there are three possible sources of significant error, all of which relate to inherent limitations in the water channel setup.

First, imprecision in the flow speed measurement may have resulted in variation of the dimensionless groups across experiments. In this work, flow speed is measured by a point probe with a resolution of ± 1.5 cm/s. Depending on which experiment is being conducted, this corresponds to a possible error in the flow speed of between 5.4% and 9.1%. The impact of this quantization-type error is particularly visible in the normalized flow speeds of Table 6.

Second, camera lens distortion effects can have a nontrivial effect on results. In particular, the approximations of Eq. (22) are accurate when the tracking targets appear near the center of the frame. Whereas lens distortion will cause them to become less accurate as the model deviates from the center of the frame, as is common with crosswind flight.

Finally, it is understood (and demonstrated in Refs. [21–23]) that the lateral stability of the model depends heavily on the achieved pitch angle. Generally, higher pitch results in greater lateral movement. Small inaccuracies in placement of the image tracking targets on the models can result in slight differences between the measured and achieved pitch angle across model scales. This in turn can lead to inconsistencies between model behavior at different scales.

6 Conclusions

This paper presented a framework for lab-scale control and measurement of crosswind airborne wind energy systems. The framework is capable of simultaneous control of altitude, pitch, and roll, while measuring important variables upon which energy generation depends. The paper followed with a detailed discussion of crosswind flight performance across a range of model scales and flow speeds, including experimental validation of the dynamic scaling laws derived in this and previous work. Specifically, a dynamic model-based dimensional analysis from Ref. [23] suggested that properly scaled plant and controller parameters will lead to dynamic equivalence across all model scales during closed-loop control of crosswind flight. It was shown that the dynamics scaled properly across a range of available model scales, within experimental uncertainty.

Funding Data

- Entitled Collaborative Research: Self-Adjusting Periodic Optimal Control with Application to Energy-Harvesting Flight, National Science Foundation (Grant No. 1538369).

References

[1] X Development LLC, 2017, "Makani Power," X Development LLC, Mountain View, CA, accessed Dec. 18, 2017, http://www.google.com/makani/

[2] Arriaga, M., Caizares, C. A., and Kazerani, M., 2013, "Renewable Energy Alternatives for Remote Communities in Northern Ontario, Canada," IEEE Trans. Sustainable Energy, **4**(3), pp. 661–670.

[3] Pentland, W., 2012, *Lockheed Gambles on Green Generators for U.S. Military*, Forbes, New York.

[4] Kitenergy, 2017, "KITEnrg," Kitenergy, Turin, Italy, accessed Dec. 18, 2017, http://www.kitenergy.net/

[5] ALTAEROS, 2017, "The Next Transformation in Rural Infrastructure Efficiency," Altaeros Energies, Somerville, MA, accessed Dec. 18, 2017, http://www.altaerosenergies.com/

[6] Ampyx Power, 2017, "The Energy of Tomorrow," Ampyx Power, The Hague, The Netherlands, accessed Dec. 18, 2017, https://www.ampyxpower.com/

[7] EnerKite, 2017, "Flugwindkraftanlagen," EnerKite, Kleinmachnow, Germany, accessed Dec. 18, 2017, http://www.enerkite.de/

[8] Windlift, 2017, "Windlift," Windlift, Raleigh, NC, accessed Dec. 18, 2017, http://windlift.com/

[9] KiteGen, 2017, "KiteGen Research," KiteGen, Torino, Italy, accessed Dec. 18, 2017, http://www.kitegen.com/en/

[10] Loyd, M., 1980, "Crosswind Kite Power," J. Energy, **4**(3), pp. 106–111.

[11] Williams, P., Lansdorp, B., and Ockels, W., 2008, "Optimal Crosswind Towing and Power Generation With Tethered Kites," J. Guid., Control, Dyn., **31**(1), pp. 81–93.

[12] Ilzhofer, A., Houska, B., and Diehl, M., 2007, "Nonlinear MPC of Kites Under Varying Wind Conditions for a New Class of Large-Scale Wind Power Generators," Int. J. Robust Nonlinear Control, **17**(17), pp. 1590–1599.

[13] Fagiano, L., Zgraggen, A., Morari, M., and Khammash, M., 2014, "Automatic Crosswind Flight of Tethered Wings for Airborne Wind Energy: Modeling, Control Design, and Experimental Results," IEEE Trans. Control Syst. Technol., **22**(4), pp. 1433–1447.

[14] Massimo, C., Fagiano, L., and Milanese, M., 2010, "High Altitude Wind Energy Generation Using Controlled Power Kites," IEEE Trans. Control Syst. Technol., **18**(2), pp. 279–293.

[15] NikpoorParizi, P., and Vermillion, C., 2016, "Combined Plant and Controller Performance Analysis and Optimization for an Energy-Harvesting Tethered Wing," American Control Conference (ACC), Boston, MA, July 6–8, pp. 4089–4094.

[16] Kehs, M., and Vermillion, C., 2015, "Maximizing Net Power Output of an Airborne Wind Energy Generator Under the Presence of Parametric Uncertainties," ASME Paper No. DSCC2015-9764.

[17] Vermillion, C., and Glass, B., 2014, "Development of Full-Scale Experimental Validation of a Rapid Prototyping Environment for Plant and Control Design of Airborne Wind Energy Systems," ASME Paper No. DSCC2014-5907.

[18] Vermillion, C., and Glass, B., 2014, "Evaluation of a Water Channel-Based Platform for Characterizing Aerostat Flight Dynamics: A Case Study on a Lighter-Than-Air Wind Energy System," AIAA Paper No. 2014-2711.

[19] Fagiano, L., Huynh, K., Bamieh, B., and Khammash, M., 2013, "Sensor Fusion for Tethered Wings in Airborne Wind Energy," American Control Conference (ACC), Washington, DC, June 14–19, pp. 2884–2889.

[20] Hably, A., and Dumon, J., 2016, "Control of an Airborne Wind Energy System With a Magnus Effect," American Control Conference (ACC), Boston, MA, July 6–8, pp. 4978–4983.

[21] Deese, J., Muyimbwa, T., Deodhar, N., and Vermillion, C., 2015, "Lab-Scale Characterization of a Lighter-Than-Air Wind Energy System—Closing the Loop," AIAA Paper No. 2015-3350.

[22] Deodhar, N., and Vermillion, C., 2015, "A Case Study in Experimentally-Infused Plant and Controller Optimization for Airborne Wind Energy Systems," American Control Conference (ACC), Chicago, IL, July 1–3, pp. 2371–2376.

[23] Deodhar, N., Bafandeh, A., Deese, J., Smith, B., Muyimbwa, T., Vermillion, C., and Tkacik, P., 2017, "Lab-Scale Flight Characterization of a Multiethered Aerostat for Wind Energy Generation," AIAA J., **55**(6), pp. 1823–1832.

[24] Cobb, M., Fathy, H., and Vermillion, C., 2016, "Lab-Scale Experimental Crosswind Flight Control System Prototyping for an Airborne Wind Energy System," ASME Paper No. DSCC2016-9737.

[25] Otsu, N., 1979, "A Threshold Selection Method From Gray-Level Histograms," IEEE Trans. Syst., Man, Cybern., **9**(1), pp. 62–66.

[26] Buckingham, E., 1914, "On Physically Similar Systems; Illustrations of the Use of Dimensional Equations," Phys. Rev., **4**, pp. 345–376.